Gas-driven subharmonic waves in a vibrated two-phase granular material

Jean-Philippe Matas, Jun Uehara, R. P. Behringer

EPJ E
Soft Matter
www.epj.org

Eur. Phys. J. E **25**, 431–438 (2008) DOI: 10.1140/epje/i2007-10310-5

Gas-driven subharmonic waves in a vibrated two-phase granular material

J.-P. Matas, J. Uehara and R.P. Behringer

EDP SCIENCES
Società Italiana Di Fisica
Springer

Eur. Phys. J. E **25**, 431–438 (2008)
DOI 10.1140/epje/i2007-10310-5

THE EUROPEAN PHYSICAL JOURNAL E

Gas-driven subharmonic waves in a vibrated two-phase granular material

J.-P. Matas[a], J. Uehara, and R.P. Behringer[b]

Department of Physics & Center for Nonlinear and Complex Systems, Duke University, Durham NC, 27708-0305, USA

Received 9 October 2007 and Received in final form 24 January 2008
Published online: 18 April 2008 –

Abstract. Vibrated powders exhibit striking phenomena: subharmonic waves, oscillons, convection, heaping, and even bubbling. We demonstrate novel rectangular profile subharmonic waves for vibrated granular material, that occur uniquely in the two-phase case of grains, and a fluid, such as air. These waves differ substantially from those for the gas-free case, exhibit different dispersion relations, and occur for specific shaking parameters and air pressure, understandable with gas-particle flow models. These waves occur when the gas diffusively penetrates the granular layer in a time comparable to the shaker period. As the pressure is lowered towards P=0, the granular-gas system exhibits a Knudsen regime. This instability provides an opportunity to quantitatively test models of two-phase flow.

PACS. 45.70.-n Granular systems – 47.20.-k Flow instabilities

1 Introduction

Vibrated powders are relevant to many practical processes, such as transport of materials or fluidization of pharmaceutical powders [1]. Previous studies on vibrated granular media have evidenced different types of surface instabilities: these instabilities are either gas dependent [2–5] (*i.e.* convection, heaping or bubbling) or arising solely from the interactions between grains [6–8] and possibly walls. Whereas the instabilities falling in the first category generally induce a fluid-like behavior of the grains (with for example large-scale mean motion or random bubbling), it has been observed that the purely granular instabilities generally lead to subharmonic waves. In order to better understand what makes the gas relevant to granular instabilities, we investigated what happens for reduced gas pressure, at the frontier between both regimes. We discovered for these conditions a distinctly different type of subharmonic instability, in which grains are not fluidized in the sense described above, but which is however gas driven.

The paper is organized as follows: we present in the second part a description of the experimental conditions for which this new instability could be observed, and of amplitude and wavelength measurements carried out on the instability. In the third part, we model gas flow through the granular layer, and derive a relevant diffusive length for our experimental conditions. In part four we confront the results of this analysis with experimental measurements.

2 Experimental observations

Our experimental set-up consists of a closed Plexiglas cell (interior horizontal dimensions 1 cm by 4 cm, and 6 cm vertical) driven vertically by an electromagnetic shaker. The driving is harmonic: $z = A_p \cos \omega t$ with dimensionless acceleration $\Gamma = A_p \omega^2/g$ (g the gravitational acceleration). We drive the cell in the range $\Gamma \leq 10$, $A_p \leq 1$ cm, and $\omega/2\pi \leq 500$ Hz. The top of the cell is connected to a reservoir tank (volume $V \approx 30$ l) and to a differential pressure gauge. By connecting the cell and tank system to a vacuum pump, we can vary the pressure in the range 0.01 Torr $< P <$ 100 Torr. The reservoir tank ensures that pressure in the system remains stable over the course of our measurements. We use relatively cohesionless powders: glass spheres with diameters d in the range 50 μm $< d <$ 100 μm. The layer heights span 1 mm $\leq H \leq$ 2 cm, *i.e.* a thickness of 10 to more than 400 particles depending on particle size. We image flow patterns by high-speed video, strobing and conventional video.

When the glass spheres are vibrated at atmospheric pressure, classical heaping associated with convection is observed. This is true for all values of the layer thickness H. When the pressure, P, is decreased, heaping ceases and we observe a subharmonic instability exhibiting a striking aspect: rectangular blocks form standing waves oscillating

[a] *Present address:* LEGI-UJF, BP53 38041 Grenoble France, e-mail: matas@hmg.inpg.fr
[b] Correspondence and requests for materials should be addressed to bob@phy.duke.edu.

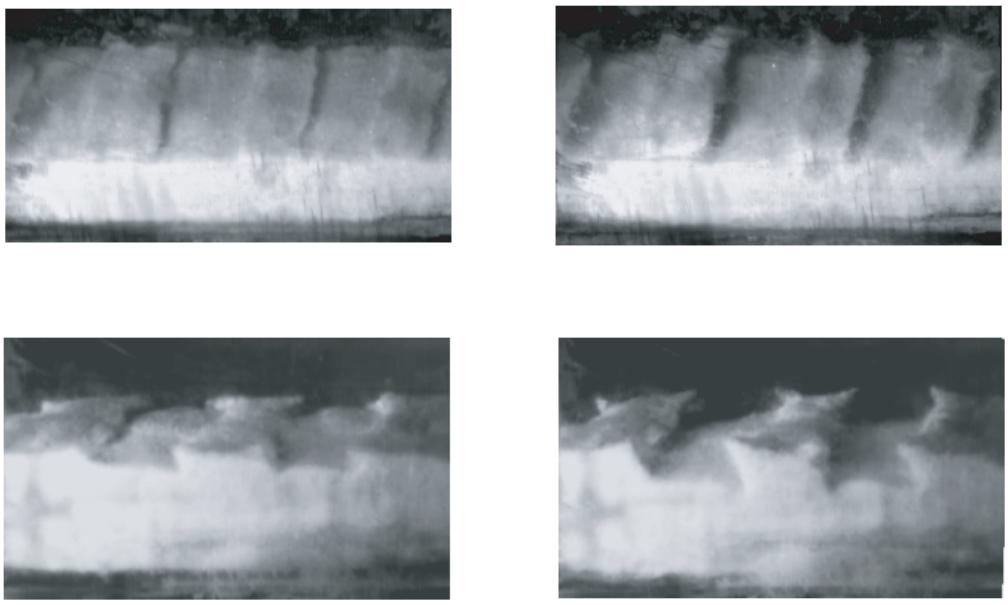

Fig. 1. Top two images: standing waves observed for $f = 35\,\mathrm{Hz}$, $P = 0.15\,\mathrm{Torr}$. Bottom two images: same conditions, side view.

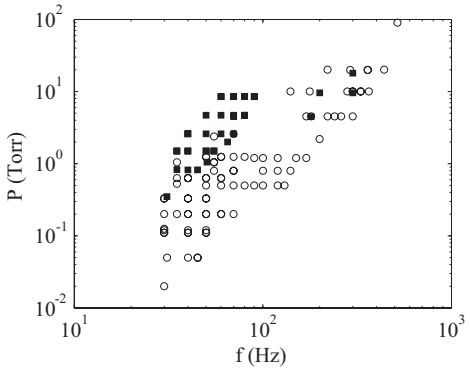

Fig. 2. Values of pressure P and frequency f, for which rectangular cross-section standing waves could be observed; o: $1 < H < 1.5\,\mathrm{cm}$; ■: $1.5 < H < 2\,\mathrm{cm}$. The waves are only visible over a range of frequencies, which shifts towards larger values with increasing P.

at half the excitation frequency (see Fig. 1 for a picture of these blocks). A closer look shows that the blocks are actually wider at the top than at their base. Their surface is slightly concave when they reach their maximum amplitude, and slightly convex when they are at their lowest position (Fig. 1). The unique feature of this instability resides in the very sharp edges of the blocks, even when the standing waves have an amplitude small compared to their wavelength (top and bottom left pictures of Fig. 1). The grains visible at the surface of the layer only have a vertical motion, and there is no visible sloshing motion as in other instabilities observed for larger grains [6–8]. If P is further decreased, the pattern disappears, indicating that the gas plays a crucial part in the instability. For a given P, there always exists a window of frequencies for which this instability can be observed, but this window depends on pressure: when P is increased, the instability is observed for larger frequencies (see phase diagram of Fig. 2). The pressure-frequency relation also depends on the thickness of the granular layer: for a given P, the frequency has to be decreased to recover the instability if the layer thickness H is increased. We note that for very thin layers of grains ($H < 20\ d$) this new instability could not be observed: in this case we observe either heaping (if $P > 0.01\,\mathrm{Torr}$), or if the pressure is lowered enough, the subharmonic sloshing instabilities observed in systems of larger grains [6–8], and their associated geometrical patterns (typically for $P < 0.01\,\mathrm{Torr}$).

Hereafter, we will focus on the rectangular cross-section standing waves of Figure 1. These waves occur for accelerations of the bottom plate larger than $\Gamma_c \sim 3$, and they can persist up to $\Gamma \sim 5$. When the waves occur, the granular layer is divided into alternately expanding and contracting bands: the sketches of Figure 3 represent the motion of the blocks relative to the bottom plate position. A thin gap can be observed at the bottom of the layer for part of a period: this gap is maximum when the bottom plate reaches its maximum descending velocity. The gap is always much smaller than the amplitude of the waves, and is spatially uniform: the amplitude of the waves being of the order of the layer thickness, this suggests that from band to band, there are strong horizontal variations of the density of the granular layer when the waves occur. In order to describe more precisely the wave motion, we have measured the positions of the surface of the waves and of the bottom of the layer as a function of time, and we compare them with the plate position. The results, shown in Figure 4, indicate how the subharmonic motion of the waves is synchronized with the motion of the bottom plate. The bottom gap (bottom graph of Fig. 4) is zero only during half a period of plate motion, when the plate is going up ($v_p > 0$).

We could observe that for low frequencies ($f < 50\,\mathrm{Hz}$) waves were in most cases oriented as in Figure 1: they

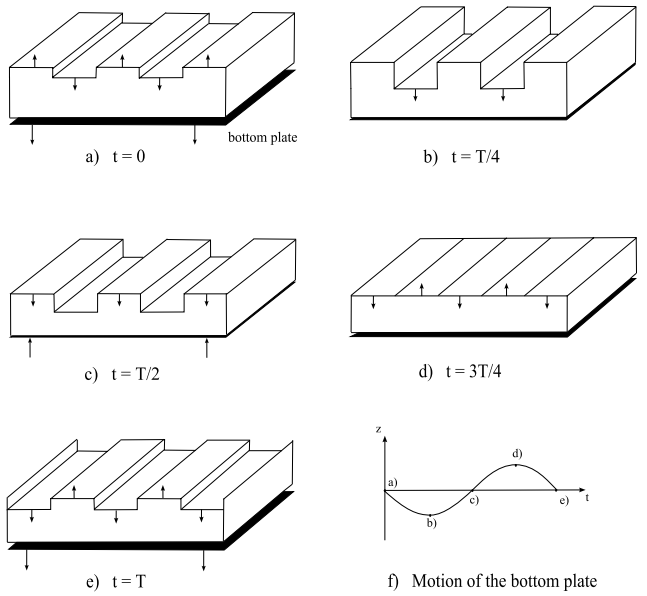

Fig. 3. a-f) Sketches showing the motion of the waves as a function of the bottom plate position. The period T is the period of the shaker motion; it corresponds to half the period of the wave motion. The largest gap between the granular layer and the shaker is observed when the plate is moving down (positions a and e).

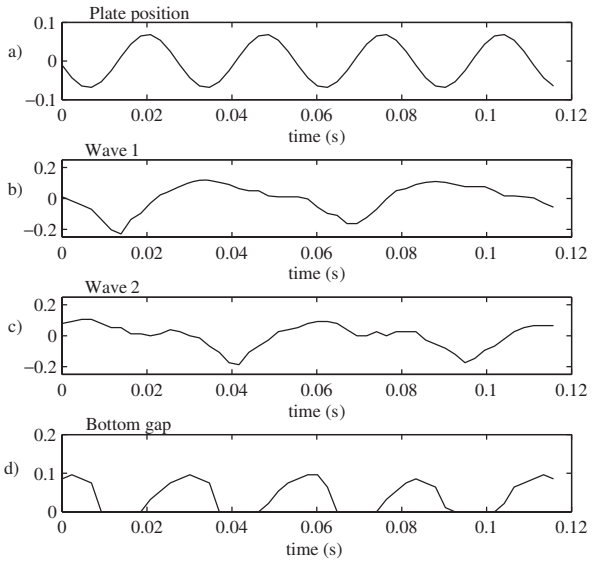

Fig. 4. Simultaneous variations as a function of time of: a) plate position; b) and c) surface of two adjacent waves in lab frame; d) thickness of the bottom gap. Lengths are in cm, time in s. Experimental conditions are $f = 36$ Hz, particle diameter 60 mm, $P = 0.15$ Torr, dimensionless plate acceleration $\Gamma = 3.5$.

are perpendicular to the largest side of the cell (4 cm), and parallel to its shorter side (1 cm). For larger frequencies, the alignment tends to be less systematic. Tests carried out with other cells of different dimensions showed the same trend, with waves generally aligned parallel to the smaller side of the cell for low frequencies. The wave nearest to the end wall tends to have a slightly smaller

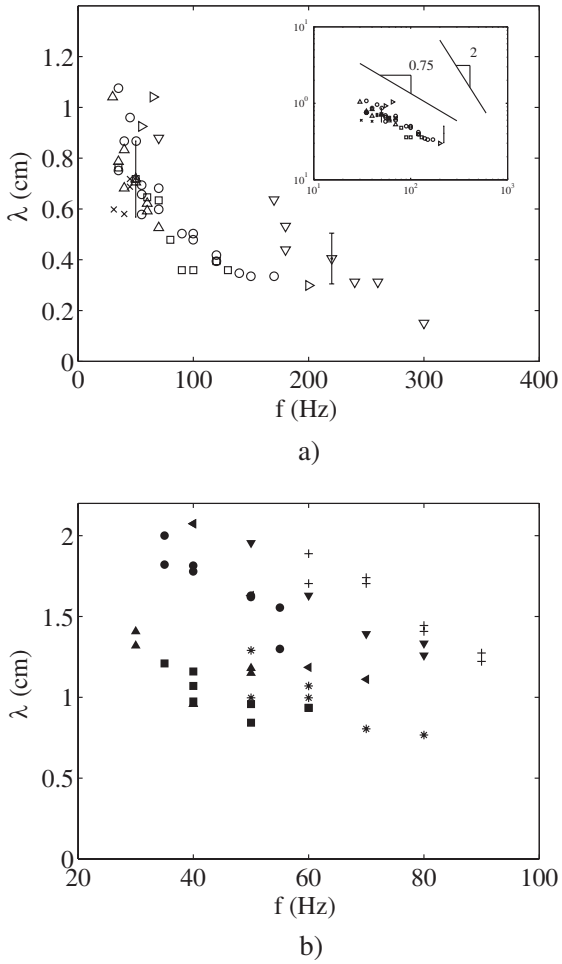

Fig. 5. Dispersion relation λ (cm) *vs.* f (Hz) a) 60 μm particles: $\times$: $P = 0.4$ Torr; $\triangle$: $P = 1.6$ Torr; $\square$: $P = 4.2$ Torr; $\circ$: $6.6 < P < 9.9$ Torr; $\triangleright$: $P = 18$ Torr; $\triangledown$: $P = 37$ Torr. Inset: power law fit; b) 80 μm particles: $\blacktriangle$: $P = 2.7$ Torr; $\blacksquare$: $P = 5.2$ Torr; $*$: $P = 10$ Torr; $\bullet$: $P = 12$ Torr; $\blacktriangleleft$ $P = 21$ Torr; $\blacktriangledown$: $P = 39$ Torr; $+$: $P = 70$ Torr.

amplitude, likely due to friction. It must be noted that the position of the first wave edge does not seem to be affected by the distance to the end wall: when averaged over several experiments, different configurations can be encountered, with sometimes the first wave edge very close to the wall and sometimes this first edge distant from half a wavelength from the wall. This suggests that the wave pattern is not resonant.

The wavelength λ, of the standing waves was measured as a function of frequency by visualization from top of the cell. The results of these measurements for several values of the pressure P are shown in Figure 5. Figure 5a shows the wavelength for 60 μm particles; λ decreases with increasing frequency. It can be seen that except for the largest pressure investigated ($P = 37$ Torr, symbol $\triangledown$), λ depends only weakly on pressure. In Figure 5b, measurements show that the wavelength is larger for 80 μm particles than for 60 μm particles. As for the smaller particles, λ for the 80 μm particles decreases with increasing frequency. Also, for $P < 10$ Torr the wavelength is rela-

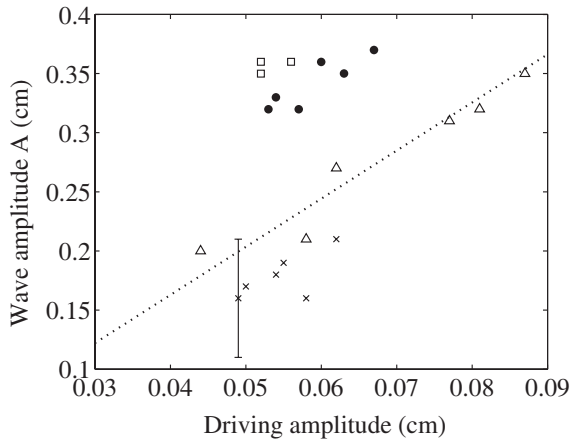

Fig. 6. Data for the wave amplitude A (in cm), as a function of the driving amplitude A_p (in cm), for $f = 40\,\mathrm{Hz}$ and for different values of the pressure; ×: $P < 8\,\mathrm{Torr}$; △: $P = 16\,\mathrm{Torr}$; •: $P = 25\,\mathrm{Torr}$; □: $P = 33\,\mathrm{Torr}$. The dotted line goes through the origin. Particle diameter is 60 microns. Wave amplitude is proportional to driving amplitude.

tively independent of pressure (symbols ▲ and ■), but for $P > 10\,\mathrm{Torr}$, λ depends significantly on P; specifically, it increases with increasing pressure. A fit of the low-pressure values for the 60 μm particles, using the data for which the wavelength is independent of P, gives a dispersion relation $\lambda(\omega)$ satisfying $\lambda \propto \omega^{-\nu}$, with $1/2 \leq \nu \leq 3/4$ (see inset of Fig. 5a). This exponent is markedly different from the one observed in classical $P = 0$ subharmonic instabilities [6] where $\nu \approx 2$.

We also carried out measurements of the amplitude, A, of the waves. In Figure 6, we present data for A, as a function of the driving amplitude, A_p, for various pressures and a fixed frequency of 40 Hz. A is taken here as the maximum vertical distance between the tops of two adjacent blocks. These measurements, in particular the values for $P = 16\,\mathrm{Torr}$ fitted by the dotted line, indicate that A is proportional to the driving amplitude of the shaker. The data of Figure 6 also show that A increases when the pressure is increased. In addition, for this frequency and range of pressures, A is of the same order of magnitude as the wavelength, λ (for instance, as in the images of Fig. 1). However, when the frequency is increased, the amplitude strongly decreases; for frequencies larger than 60 Hz, A becomes much smaller than λ, and we could not carry out amplitude measurements in this range.

3 A model for gas flow

What is the physics underlying this instability? Although a complete analysis of two-phase grain-gas flow [9] is beyond the scope of this study, we can discuss the different mechanisms at the origin of grain motion, and try to offer a scenario for the instability. We argue that the granular medium is mainly subject to two different forces:

– The contact force exerted by the bottom plate. This force can only act when the bottom gap is zero. Its corresponding acceleration is of order $a_1 \sim A_p\omega^2$ with A_p the amplitude of plate motion. When the instability occurs, $a_1 \sim 3g$ or larger.
– The drag force due to gas flow: we model the gas flow in the vertical direction, z, by taking into account gas diffusion in a fixed granular matrix. The gas velocity v relative to the grains is described by Darcy's law: $v = -(\gamma/\mu)\partial P/\partial z$, with μ the gas viscosity and γ the permeability; γ is well described by $\gamma = d^2\phi^3/[150(1-\phi)^2]$, where ϕ is the porosity. We consider a fixed granular matrix through which gas flows at speeds that are typical of the shaker velocities, $v \sim A_p\omega$. This estimate is based upon the data of Figure 4 showing that the different phases of the waves are not in phase with the plate: for at least the upper part of the layer the relative speeds are not vastly different from the overall shaker speed. The resulting pressure gradient would then be $|\,\mathrm{grad}\,P| \approx A_p\omega\mu/\gamma$, and this Darcian drag would result in an acceleration $a_2 = |\,\mathrm{grad}\,P|/\rho_g = A_p\omega\mu/\gamma\rho_g$ with ρ_g the density of the granular layer. For $d = 80\,\mu\mathrm{m}$, $\rho_g = 1.5\,\mathrm{g/cm^3}$, $A_p\omega = 50\,\mathrm{cm/s}$, and $\mu = 1.8\,10^{-4}\,\mathrm{g/cm\,s}$ (viscosity of air), this gives an estimate of acceleration a_2 larger than $5g$. The magnitude of this acceleration is one reason why the subharmonic waves seen here differ substantially from those reported by Melo *et al.* [6].

We expect gravity and friction with the walls to be weak compared to the above contributions. The grains appear to move collectively only in the vertical direction, no sloshing or circulating motion is observed, and relative velocities between grains are small. These observations could be made by fast imaging visualization at the surface of the material and for grains close to the transparent walls of the cell: we assume that the absence of sloshing and circulation can be extended to the bulk of the material. Based upon the apparent motion of the grains, we therefore assume that the effect of collisions between grains is not among the principal driving forces. Put differently, the difference between the present waves, and those reported by Melo *et al.* [6] is that in our case, gas flow and drag (acceleration a_2), rather than inter-granular collisions are the dominant physical processes.

In order to go further and quantitatively compare the experimental acceleration of the granular layer with accelerations a_1 and a_2, we first need to model gas flow. In the following simplified analysis, only the effect of grains on the gas is modelled: the granular layer is assimilated to a fixed porous medium through which an oscillating gas flow is taking place. Grain motion due to the resulting drag on the porous layer will be discussed in Section 4. We therefore investigate time, length and pressure scales for oscillatory Darcian flow in a *rigid* porous layer, subject to periodically forced flow, with vertical velocity $v(H,t) = u_0\exp(i\omega t)$ at the upper boundary (we take $u_0 = A_p\omega$) and an opposing impermeable boundary. The gas dynamics are contained in Darcy's law, plus the mass continuity equation for the gas: $\partial_t(\phi\rho) + \nabla.(\rho v) = 0$,

where ρ is the gas density. In line with experimental observations showing a vertical motion of the grains, we assume that gas velocity is vertical (normal to the layer), and neglect the horizontal component of velocity in this analysis. Pressure variations are related to density variations through the compressibility, $\kappa : \delta\rho = \rho\kappa\delta P$. Here, we do not distinguish between the case of isothermal or adiabatic compressibility, which both vary as $C_\kappa P^{-1}$, and which differ only by an $O(1)$ constant, C_κ. Then, both v and P satisfy a diffusion equation [4,10],

$$D\partial_z^2 v - \partial_t v = 0, \tag{1}$$

where the Darcian diffusivity, $D = \gamma/(\kappa\mu\phi) \sim d^2P/\mu$, grows with pressure and with particle size. We carry out a spatial analysis of the problem (in the vertical direction), and look for normal mode solutions of this equation oscillating at a frequency ω and with a wave number $k(\omega)$. The dispersion relation derived from (1) is $Dk^2 = -i\omega$, which gives $k = (1-i)(\omega/2D)^{1/2} = (1-i)(\omega\kappa\mu\phi/2\gamma)^{1/2}$. Taking boundary conditions into account, we find solutions for the gas flow which have the form

$$v(z,t) = u_0 \frac{\sinh kz}{\sinh kH} e^{i\omega t}.$$

The origin of z has been taken at the bottom plate. This analysis yields a penetration depth λ_p given by

$$\lambda_p = 1/\operatorname{Re}(k) = (2D/\omega)^{1/2} = (2\gamma/\kappa\mu\phi\omega)^{1/2}. \tag{2}$$

This length represents the typical depth to which gas penetrates in the granular layer during oscillations: it logically increases with the permeability γ (*i.e.* with particle size), and decreases with increasing frequency. This points to a necessary condition for grain-gas coupling: one expects the waves to be strongest when the diffusion length λ_p is of the order of the granular layer thickness H. If λ_p is small relative to H, the gas does not pass through the layer but only diffuses at its surface; if λ_p is large relative to H, there is little coupling between the grains and gas.

In order to emphasize this point we introduce $Q = H/\lambda_p = (\kappa\mu\phi\omega H^2/2\gamma)^{1/2}$ as the key parameter. The mean pressure difference across the layer can be calculated from the gas velocity profile: $\Delta P = [u_0/kD\kappa\phi]\tanh(kH/2) = [u_0 H/QD\kappa\phi]\tanh(Q/2)$. If $Q \ll 1$, then $\lambda_p \gg H$: the gas easily moves into the layer, and $\Delta P \propto Q^2$ is small. In this case the gas velocity decreases linearly inside the granular medium; we have $v(z,t) \sim u_0(z/H)e^{i\omega t}$. As Q grows, ΔP also grows; when $Q \geq 1$, ΔP varies as Q. When $Q \gg 1$, $\lambda_p \ll H$, the flow penetration is slight, leading to gas penetration and waves that are limited to the surface. In this case, the gas velocity inside the granular layer decreases exponentially:

$$v(z,t) = u_0 \cos[\omega t - (H-z)/\lambda_p]\, e^{-(H-z)/\lambda_p}.$$

Since Q increases as ω/P, equivalent values of Q occur for higher frequencies at higher pressures. More precisely, the condition that waves are best observed if $\lambda_p \sim H$ is equivalent to setting $Q \sim 1$. This indicates that the effects of diffusive penetration will be strongest around $\omega \sim 2\gamma P/\mu\phi H^2$, *i.e.* around a frequency increasing with P. This trend is observed experimentally for the standing waves of Figure 1 (see the data of Fig. 2), although the experimental increase of P with the frequency suggests a steeper increase than a linear dependence. The scaling $\omega \sim H^{-2}$ shows that when the thickness is increased the frequency is shifted to lower values. This tendency is consistent with experiments: for a fixed pressure, larger thicknesses lead to waves occurring at smaller frequencies (comparison between empty and filled symbols of Fig. 2).

It is interesting to ask if the diffusive length scale, λ_p, is related to the observed wavelength. If the instability is caused by the drag generated by air flow (acceleration a_2), the distance between blocks should not be much larger than λ_p: if two descending blocks were separated by a distance larger than λ_p, a third descending block could be expected to appear between them. If on the contrary two descending blocks were separated by much less than λ_p, gas would diffuse laterally in the block separating them and the descending blocks would then merge. If λ_p provides an appropriate scale factor for the wavelength λ of the waves, we expect $\lambda \propto \lambda_p \propto (D/\omega)^{1/2} \propto (P/\omega)^{1/2}$. An increase of the wavelength with pressure, as well as a decrease with the frequency is indeed observed for the larger particles in Figure 5b.

However, the experimental data of Figure 5a show that for the smaller particles, and in particular smaller pressures, the wavelength becomes independent of pressure. We interpret this as the signature of a crossover to a Knudsen regime, as the mean free path of a gas molecule l becomes of the order of particle size d. Then, gas molecules become increasingly more likely to collide with a grain than with other gas molecules, an effect that has been proposed [4] to limit heaping at low (but not zero) pressure. For instance, at $P = 100\,\mathrm{Torr}$ we estimate that $l \approx 0.7\,\mu\mathrm{m}$ while at $P = 1\,\mathrm{Torr}$ we have $l \approx 70\,\mu\mathrm{m}$, which is typically our particle size. If diffusion is set by collisions of molecules with grains rather than with each other, the diffusivity used previously would no longer be valid. D in the Knudsen regime should vary as $D_K = Cv_T d$, where v_T is the thermal velocity of the gas molecules, and C is a constant [4].

We construct a simple cross-over expression between the Darcian and Knudsen regimes by writing the diffusivity $D = \gamma/(\kappa\mu\phi)$ as a function of the mean free path l through the expression for the viscosity $\mu = nmlv_T/3$ (n=number of molecules per unit volume, m = molecule mass and v_T = thermal velocity). After simplification, we obtain

$$D = \left[\pi\phi^2/(150(1-\phi)^2)\right] v_T d^2/l. \tag{3}$$

As l grows, the ordinary expression for l must be modified to account for collisions of molecules with grains rather than with each other. We estimate the generalized mean free path l_g by noting that l_g^{-1} is the scattering area per unit volume for a gas molecule, hence

$$l_g^{-1} \approx 2^{1/2} n\sigma + G(3/2)(1-\phi)/d,$$

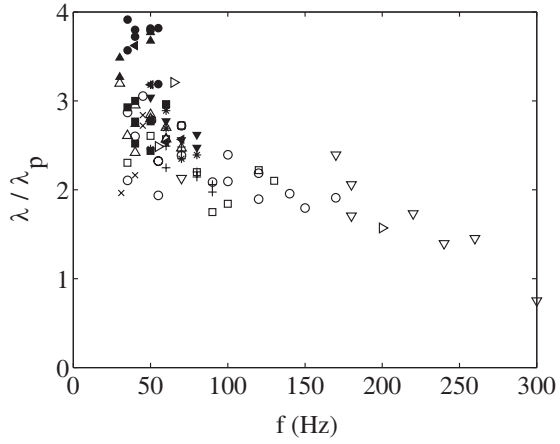

Fig. 7. Data for the scaled wavelength, λ/λ_p, *vs.* frequency f (in Hz); 60 μm particles: $\times$: $P = 0.4$ Torr; $\triangle$: $P = 1.6$ Torr; $\square$: $P = 4.2$ Torr; $\circ$: $6.6 < P < 9.9$ Torr; $\triangleright$: $P = 18$ Torr; $\triangledown$: $P = 37$ Torr; 80 μm particles: $\blacktriangle$: $P = 2.7$ Torr; $\blacksquare$: $P = 5.2$ Torr; $*$: $P = 10$ Torr; $\bullet$: $P = 12$ Torr; $\blacktriangleleft$: $P = 21$ Torr; $\blacktriangledown$: $P = 39$ Torr; $+$: $P = 70$ Torr.

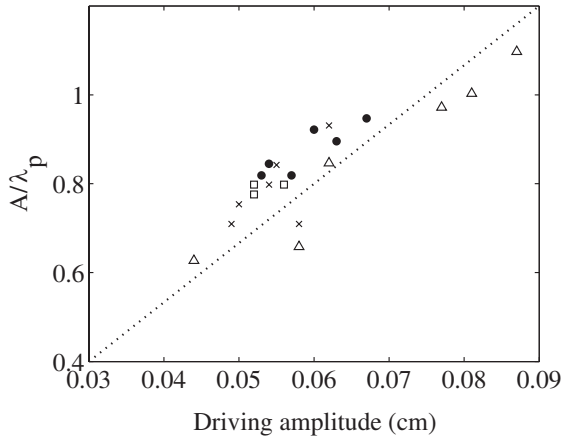

Fig. 8. Data for the wave amplitude A (in cm) scaled by the diffusive length λ_p, as a function of the driving amplitude A_p (in cm), for $f = 40$ Hz and for different values of the pressure; $\times$: $P < 8$ Torr; $\triangle$: $P = 16$ Torr; $\bullet$: $P = 25$ Torr; $\square$: $P = 33$ Torr. The dotted line goes through the origin. Particle diameter is 60 μm. The data of Figure 6 is collapsed.

where σ is the cross-section for molecular collisions [11], and G is an $O(1)$ constant. The first term accounts for collisions with other gas molecules, and the second term accounts for collisions with grains of diameter d in a granular material of porosity ϕ. The generalized diffusivity D_g follows by replacing d/l in (3) with $d/l_g \approx 2^{1/2} n\sigma d + (3/2)G(1-\phi)$. The precise numerical factors in this expression, in particular G, would require a more detailed calculation, but for the present purposes this simple expression is adequate. The generalized diffusive length scale is then given by $\lambda_p = (2D_g/\omega)^{1/2}$. This length scale behaves as $\lambda_p(P,\omega) \sim (P/\omega)^{1/2}$ for pressures in the Darcian regime, but as the system enters the Knudsen regime it becomes independent of P: $\lambda_p(P,\omega) \sim \omega^{-1/2}$.

4 Comparison with experimental data

We see in Figure 7 that when the wavelength λ of Figure 5 is scaled by λ_p the wavelength data for all pressures collapse reasonably well on a single curve. In addition, the data for different particle sizes also collapse on the same curve, indicating that the scaling $\lambda \sim D^{1/2}$ is adequate. Here, we use a value of $G = 10$ for the Knudsen contribution, a value consistent with a related estimate in studies of heaping at low P [4]. However the dependence on ω is not completely captured in the scaling by $\omega^{-1/2}$: rather, the experimental data exhibit a scaling $\lambda \propto \omega^{-3/4}$ (Fig. 5b). This is not surprising, since temporal behaviour in our model is only controlled by gas dynamics: grain motion, which has not been considered, might significantly affect the scaling of the dispersion relation. In spite of this discrepancy, the fact that pressure and particle diameter effects are taken into account and that the ratio λ/λ_p remains in the range 1–4 support our hypothesis

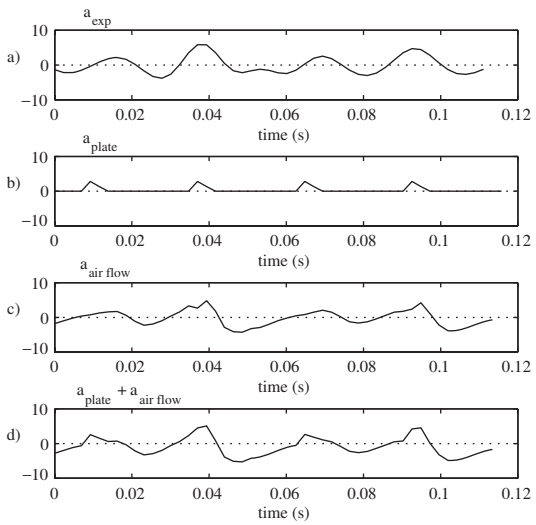

Fig. 9. a) Experimental dimensionless acceleration (units of g) as a function of time. b) Acceleration from impulsive interaction with bottom plate. c) Acceleration caused by air flow, based on generalized diffusivity. d) Sum of plate and air flow contributions. Time is in s.

that the diffusive length scale λ_p is the correct scale for this instability.

In order to test if the variations of the amplitude of the waves with pressure are consistent with the change of diffusive length λ_p, we plot in Figure 8 the ratio of the wave amplitude to λ_p as a function of the driving amplitude. This Figure shows that λ_p captures well the variations of the amplitude with pressure, with the data of Figure 6 falling on a single curve. This scaling can be interpreted as indicating that the diffusive length controls the depth affected by diffusion, and therefore the height of granular material expected to take part in the waves.

With this modelling of gas flow and values for the diffusivity in the Knudsen and Darcian regime, we can now take a closer look at the physics of the instability and evaluate its driving forces. In order to abandon the approximation that grains are fixed, we first need to determine how grains will be set in motion by the diffusive gas flow and the bottom plate. Figure 9a shows the acceleration of the surface of the layer, as obtained from the experimentally measured position of Figure 4c. As argued in section 3, the main forces contributing to the motion of the layer are the impulsive force exerted by the bottom plate (acceleration a_1), and the force due to air flow (acceleration a_2). We first look at the role played by the acceleration of the bottom plate; we can neglect this contribution when the bottom gap is non zero (*i.e.* when the layer does not touch the plate, see Fig. 4d). In addition, we only consider positive values of the acceleration, since contact with the bottom plate can only push the grains upwards, and not pull them. The result is the acceleration a_{plate} of Figure 9b. Its maximum value is about 3g for the experimental conditions of Figure 4 ($f = 36\,\mathrm{Hz}$, $P = 0.15\,\mathrm{Torr}$). The acceleration a_2 contributed by air flow to grain motion is a function of the velocity of grains relative to the cell velocity, Δv: this relative velocity gives a pressure gradient as a function of the medium diffusivity D_g. The resulting acceleration is

$$a_{\text{air flow}} = \text{grad}\, P/\rho_g = -\Delta v/\kappa\phi D_g \rho_g.$$

This expression shows a strong dependence of the drag with porosity, with $a_{\text{air flow}} \sim (1-\phi)^2/\phi^3$ in the Darcian regime and $a_{\text{air flow}} \sim (1-\phi)/\phi^3$ in the Knudsen regime.

The impact of grain motion has so far been neglected in the gas flow analysis: however the large variations of porosity between when the layer is compressed and when it is expanded (Fig. 1) suggest that the feedback of grain motion on the drag associated to $a_{\text{air flow}}$ might not be negligible. The drag will be larger for lower porosity, *i.e.* when the waves are compacted, than when the waves are expanded. Porosity at time t is therefore expressed as a function of the height of the granular layer h, in order to take into account the large variations of ϕ with time: we take $(1-\phi(t))/(1-\phi_{min}) = h_{min}/h(t)$. The minimum value of the porosity is taken to be $\phi_{min} = 0.3$ when the waves reach their maximum compaction. Given the variations of h with time (measured from the data of Fig. 4c) this sets an average porosity value of $\phi_m = 0.45$, and a maximum value $\phi_{max} = 0.55$ when the waves are at their maximum expansion. The acceleration caused by air flow is then plotted in Figure 9c: it is positive when the velocity of the cell is larger than the velocity of the granular layer, *i.e.* when the grains are going down in the cell frame. This acceleration is of order 4g for the experimental conditions of Figure 4. The diffusion regime is mostly a Knudsen regime for the conditions of this Figure. Note that the use of a Darcian diffusivity would yield much larger values for this acceleration ($a \sim 25g$). The total acceleration is shown in Figure 9d, the sum of the plate and air flow contributions. It exhibits a rather good agreement with Figure 9a, with positive and negative regions of acceleration coinciding. This indicates that in spite of all the approximations, our modelling of gas flow efficiently captures the physics of the problem.

Horizontal variations have not been considered in our modelling. The strong influence of porosity on the drag evidenced in the expression for $a_{\text{air flow}}$ may provide a mechanism for the horizontal destabilization of the surface: Suppose that there is an initial wavy perturbation of the surface of the layer. A spatial porosity variation will correspond to this surface variation, with a smaller porosity (higher compaction) when the surface is lower. During the part of oscillations when air is flowing downwards drag will then be higher on the lower regions than on the higher ones, causing them to go down faster. The surface perturbation will therefore be amplified. On the contrary when air is going up this mechanism predicts that an initial wavy perturbation will be stable. A generalization of our model taking into account both spatial horizontal variations and porosity variations might then capture the unstable nature of the system.

Another aspect not covered by our model is the subharmonic response to the forcing by the bottom plate. We propose an explanation based on the combined effects of the force exerted by the plate and the air drag. It can be seen that the impulsive force from the plate at $t \approx 0.04\,\mathrm{s}$ in Figure 9b corresponds to a region of upwards gas velocity (Fig. 9c). The wave starts to rise at this moment (see Fig. 4c at $t = 0.04\,\mathrm{s}$). The following plate impulse, around $t = 0.065\,\mathrm{s}$, corresponds to a much smaller gas velocity (Fig. 9c), possibly because of the lesser compaction at this moment. The resulting total acceleration (about $2g$) is then much smaller than for the previous impulse (about $5g$). The next impulse, at $t = 0.095\,\mathrm{s}$, again coincides with a large and positive gas velocity. This enhancement of the bottom plate accceleration every two cell oscillations may be seen as driving mechanism for the subharmonic nature of the instability.

5 Conclusion

To conclude, we have shown that novel subharmonic waves with a rectangular cross-section occur in vertically shaken granular materials, and depend in an essential way on the presence of gas. We understand the parameter range where these waves occur in terms of gas diffusion through a porous medium, including both Darcian (viscous) and Knudsen regimes. These waves differ from the much-studied purely granular subharmonic waves [6–8], of which oscillons [7] may be the best known state. Significant challenges remain: what are the details of the gas flow within/near the material; how does this couple to dilation and compaction of the grains; and finally, what causes the formation of the distinctly rectangular profile of the waves?

This work has been supported by Oriel Therapeutics, Inc, and by the North Carolina Biotechnology Center. We appreciate helpful discussions with Drs. Anthony Hickey and Timm Crowder.

References

1. M.K. Taylor, J. Ginsburg, A.J. Hickey, F. Gheyas, AAPS PharmSciTech **1**, article 18 (2000).
2. S. Fauve, S. Douady, C. Laroche, Europhys. Lett. **8**, 621 (1989).
3. H.K. Pak, E. Van Doorn, R.P. Behringer, Phys. Rev. Lett. **74**, 4643 (1995).
4. R.P. Behringer, E. Van Doorn, R.R. Hartley, H.K. Pak, Granular Matter **4**, 9 (2002).
5. H.K. Pak, R.P. Behringer, Nature **371**, 231 (1994).
6. F. Melo, P.B. Umbanhowar, H.L. Swinney, Phys. Rev. Lett. **72**, 172 (1994).
7. P.B. Umbanhowar, F. Melo, H.L. Swinney, Nature **382**, 973 (1998).
8. B.C. Lewis, M.D. Shattuck, H.L. Swinney, Phys. Rev. E **63**, 041305:1-12 (2001).
9. R.R. Jackson, *The dynamics of fluidized particles* (Cambridge University Press, 2000).
10. R.G. Gutman, Trans. Inst. Chem. Eng. **54**, 174 (1976).
11. J. Jeans, *An introduction to the kinetic theory of gases* (Cambridge University Press, 1959).